JOURNAL OF SOLID STATE CHEMISTRY **141,** 576–586 (1998)
ARTICLE NO. SC988023

Structure and Property Relationships in Mixed-Conducting $Sr_4(Fe_{1-x}Co_x)_6O_{13\pm\delta}$ Materials

B. Ma,* J. P. Hodges,† J. D. Jorgensen,† D. J. Miller,† J. W. Richardson, Jr.,‡ and U. Balachandran*,[1]

**Energy Technology Division, †Materials Science Division, and ‡Intense Pulsed Neutron Source, Argonne National Laboratory, Argonne, Illinois 60439*

Received May 26, 1998; in revised form August 24, 1998; accepted August 25, 1998

Mixed-conducting ceramic oxides have potential uses in high-temperature electrochemical applications such as solid-oxide fuel cells, batteries, sensors, and oxygen-permeable membranes. The $Sr_4(Fe_{1-x}Co_x)_6O_{13\pm\delta}$ system combines high electronic/ionic conductivity with appreciable oxygen permeability at elevated temperatures. Dense ceramic membranes made of this material can be used to separate high-purity oxygen from air without the need for external electrical circuitry or to partially oxidize methane to produce synthesis gas (syngas, CO + H_2). Samples of $Sr_4(Fe_{1-x}Co_x)_6O_{13\pm\delta}$ (where $x = 0$, 0.1, 0.2, 0.333, and 0.467) were prepared by a solid-state reaction method in atmospheres with various oxygen partial pressure (p_{O_2}) and were characterized by powder X-ray diffraction, scanning electron microscopy, and electrical conductivity testing. The proportion of phase components in the samples is dependent on both cobalt content and p_{O_2}. The total conductivity increases with both temperature and cobalt substitution in the material. Current–voltage characteristics determined in a gas-tight cell indicate that a bulk effect, rather than a surface exchange effect, is the main limiting factor for oxygen permeation through membranes made of $Sr_4Fe_4Co_2O_{13\pm\delta}$ ($x = 0.333$ sample). Oxygen permeability measurements at various temperatures showed that, as expected, permeability increases with increasing temperature. At 900°C, an oxygen permeation flux of 2.5 $scc \cdot cm^{-2} \cdot min^{-1}$ was obtained from an $Sr_4Fe_4Co_2O_{13\pm\delta}$ disk membrane that was 2.9 mm thick. © **1998 Academic Press**

INTRODUCTION

Oxides with mixed electronic and ionic conductivities have received increased attention because of their applicability to high-temperature electrochemical processes (1–5), for example, their use as electrodes in solid-oxide fuel cells and, if their oxygen permeability is high enough, oxygen separation membranes. $Sr_4(Fe_{1-x}Co_x)_6O_{13\pm\delta}$ materials have not only high combined electronic and oxide-ion conductivity but also oxygen permeability that is superior to that of other reported ceramic oxides (6–11). It is an excellent candidate material as a dense membrane for separation of high-purity oxygen. In an oxygen separation reactor, oxygen can be transported from the high oxygen partial pressure (high-p_{O_2}) side to the low-p_{O_2} side under the driving force of the p_{O_2} difference, $\Delta\log(p_{O_2})$, without the need for external electrical circuitry. Balachandran *et al.* (7) demonstrated that extruded membrane tubes made of $Sr_4(Fe_{1-x}Co_x)_6O_{13\pm\delta}$ can be used for partial oxidation of methane to produce syngas (CO + H_2) in a methane conversion reactor that operates at ~ 850°C. In this type of reactor, oxygen liberated on one side of the membrane was separated from air on the other. Methane conversion efficiencies of > 98% were observed and the reactor tubes have operated in excess of 1000 h. Moreover, the oxygen flux obtained from the separation of air in this type of conversion reactor is considered commercially feasible. The use of this technology can significantly reduce the cost of oxygen separation (12).

To obtain sufficient oxygen flux, the gas separation reactor must be operated at high temperatures and substantial p_{O_2} differences. Therefore, stability of the ceramic membranes is an important issue. Previously, certain perovskite $Sr_4(Fe_{1-u}Co_u)O_{3-\delta}$ compounds have been found unsuitable for use in gas separation because they lack structural stability in highly reducing environments (13). Thermodynamic calculations can normally provide accurate data on the stability of a system. However, certain examples of discrepancies between the calculated thermodynamic stability and the actual results indicate the importance of obtaining supporting data from real systems (14).

In this paper, we report our studies on the structure and transport properties of $Sr_4(Fe_{1-x}Co_x)_6O_{13\pm\delta}$ materials. Electrical conductivity was determined at elevated temperatures in various p_{O_2} atmospheres. Oxygen permeability was measured with a gas-tight electrochemical cell. Room-temperature powder X-ray diffraction and scanning electron microscopy (SEM) experiments were also conducted to characterize the materials.

The U.S. Government's right to retain a nonexclusive royalty-free license in and to the copyright covering this paper, for governmental purposes, is acknowledged.

[1] To whom correspondence should be addressed. E-mail: u_balachandran@qmgate.anl.gov.

0022-4596/98 $25.00

EXPERIMENTAL

$Sr_4(Fe_{1-x}Co_x)_6O_{13\pm\delta}$ (with $x = 0, 0.1, 0.2, 0.333$, and 0.467) powders were prepared by a solid-state reaction method, with appropriate amounts of $SrCO_3$, $Co(NO_3)_2 \cdot 6H_2O$, and Fe_2O_3; mixing and grinding were conducted in 2-propanol with zirconia media for 10 h. After drying, the mixture was calcined in air at 850°C for 16 h, with intermittent grinding. After the final calcination, the powders were ground with an agate mortar and pestle to an average particle size of ≈ 7 μm. This resulting finely divided powder was pressed uniaxially under a 1200-MPa load into pellets that were 21.5 mm in diameter and ≈ 4 mm thick. The pellets were then sintered in air at 1200°C for 5 h and slowly cooled at $\approx 90°C \cdot h^{-1}$ to room temperature. Bulk density was determined by the Archimedean method, with 2-propanol as the liquid medium. The calculated relative density of air-sintered $Sr_4Fe_4Co_2O_{13\pm\delta}$ ($x = 0.333$) samples was $\approx 95\%$ of the theoretical value. Thin bars ca. $1 \times 5 \times 20\ mm^3$ were cut from the samples and subjected to a postannealing heat treatment in flowing argon ($p_{O_2} \approx 10^{-6}$) environment at 1100°C. The sintered pellets were polished on both sides and used for permeation tests.

Room-temperature powder X-ray diffraction data were collected with a Scintag XDS-2000 diffractometer, using $CuK\alpha_1$ radiation. A high-purity intrinsic Ge energy-dispersive detector was used to minimize background due to sample fluorescence. A continuous scan with a 2θ scanning rate of $1° \cdot min^{-1}$ and step of 0.03° was used to collect data. Rietveld analysis (15) of the X-ray diffraction data was performed using the GSAS suite of programs (16). SEM observations were conducted with a JEOL JSM-5400 scanning microscope at an accelerating voltage of 20 keV.

Total conductivity of the sample was determined by the conventional four-probe method, and ionic conductivity was measured with the electron-blocking method. Platinum wires were attached to the specimen bar to serve as current and voltage leads. Resistance of the specimen was measured with an HP 4192A LF impedance analyzer at 23 Hz. Details of the experimental configuration for measuring conductivity were reported earlier (10). A K-type thermocouple was attached to an yttria-stabilized zircona (YSZ) plate on which the sample bars were placed for the heat treatments. The thermocouple was used for both controlling and detecting the temperature of the electric furnace. Temperature tolerance within the uniform hot zone of the furnace is ±1°C. Desirable gaseous environments were obtained by flowing premixed gases through the system during the experiments.

Figure 1 shows a schematic diagram of the gas-tight electrochemical cell used in the oxygen permeation experiments. A sintered pellet of $Sr_4Fe_4Co_2O_{13\pm\delta}$ was sealed to a YSZ crucible with a Pyrex glass seal. Electrical leads (10-mil Pt wires) were separated from the YSZ crucible and $Sr_4Fe_4Co_2O_{13\pm\delta}$ disk membrane by two alumina rings. Electrodes were made on the bottom and side wall of the YSZ crucible. The bottom electrodes were used as pumping electrodes, to pump oxygen from the gas-tight cell chamber, whereas the other electrodes were used to detect the p_{O_2} inside the cell. The p_{O_2} inside the cell can be determined from the electromotive force (EMF), E, generated on the side wall of the YSZ crucible by solving

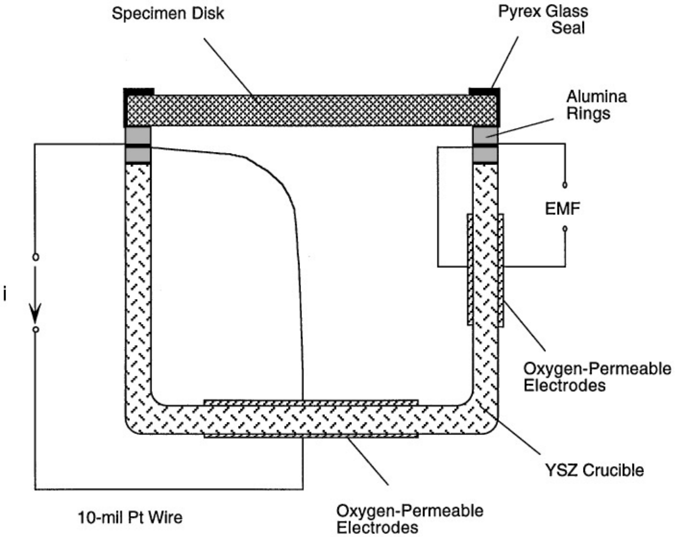

FIG. 1. Schematic drawing of cross-section view of gas-tight electrochemical cell used to measure oxygen permeability.

$$p^{II}_{O_2} = p^{I}_{O_2} \exp\left(\frac{4FE}{RT}\right), \qquad [1]$$

where $p^{II}_{O_2}$ and $p^{I}_{O_2}$ are the p_{O_2} values inside and outside the gas-tight cell, respectively. Other variables are as usual; F, Faraday's constant; R, gas constant; and T, absolute temperature. Reduced-p_{O_2} oxygen environmeents were achieved by pumping oxygen out from the gas-tight cell by using the pumping electrodes on the YSZ crucible. Oxygen permeates the $Sr_4Fe_4Co_2O_{13\pm\delta}$ disk membrane because of the p_{O_2} difference on the two sides of the membrane. Under steady-state conditions, the amount of oxygen that enters the cell by permeating the specimen disk is equal to that pumped out by the YSZ oxygen pump. Therefore, the flow of oxygen through the specimen can be determined from the current applied to the YSZ oxygen pump. The relationship of oxygen permeation flux j_{O_2} (in $mol \cdot cm^{-2} \cdot s^{-1}$) to the applied current I (in A) is given by

$$j_{O_2} = \frac{I}{4FS}, \qquad [2]$$

where S is the effective cross-sectional area of the specimen.

RESULTS AND DISCUSSION

Representative room-temperature X-ray diffraction profiles of air-sintered $Sr_4(Fe_{1-x}Co_x)_6O_{13\pm\delta}$ and, for comparison, $SrFe_{0.8}Co_{0.2}O_{13-\delta}$ perovskite are plotted in Fig. 2. Representative room-temperature X-ray diffraction profiles of the corresponding samples annealed in flowing argon are plotted in Fig. 3. Rietveld profile analysis of the diffraction data was performed to determine the phase composition of the samples synthesized. For the $Sr_4Fe_6O_{13\pm\delta}$ sample ($x = 0$) a satisfactory fit ($R_{wp} = 0.055$ and $R_p = 0.037$) to the diffraction profile was obtained (see Fig. 4) using for initial atom positions a crystallographic model of $Sr_4Fe_6O_{13}$ as reported by Yoshiasa *et al.* (17). No evidence for any secondary phases were found in this sample of $Sr_4Fe_6O_{13\pm\delta}$, indicating that this is a pure phase sample. The crystal structure of $Sr_4Fe_6O_{13}$ is particularly interesting since Fe^{3+} cations are present with three different oxygen coordinations: octahedral, trigonal bipyramidal, and square pyramidal. The structure is also layered and can be thought of as being composed of alternating blocks of $[Fe_4O_5]^{2+}$ and pervoskite-derived $[Sr_4Fe_2O_8]^{2-}$. A schematic representation of the $Sr_4Fe_6O_{13}$ crystal structure is shown in Fig. 5.

For the air-sintered $Sr_4Fe_4Co_2O_{13\pm\delta}$ sample, however, Rietveld analysis revealed a multiphase composition of approximately 70% weight fraction (wtf) $Sr_4(Fe_{1-y}Co_y)_6O_{13\pm\delta}$, 25% wtf perovskite $Sr(Fe_{1-u}Co_u)O_{3-\delta}$, and 5% wtf CoO. A lattice parameter of $a = 4.262(2)$ Å was determined for the CoO phase present in this $Sr_4Fe_4Co_2O_{13\pm\delta}$ sample. Comparison with reported lattice parameters for CoO and FeO, possessing the rock-salt crystal structure, of $a = 4.260$ and 4.307 Å (18), respectively, indicates that little, $< 8\%$, or no substitution by iron has occurred in the component CoO phase.

The lower cobalt-substituted $Sr_4(Fe_{1-x}Co_x)_6O_{13\pm\delta}$ samples, with $x = 0.1$ and 0.2, were found to be composed of approximately 95 and 90% wtf of the layered $Sr_4(Fe_{1-y}Co_y)_6O_{13\pm\delta}$ phase, respectively, and minor

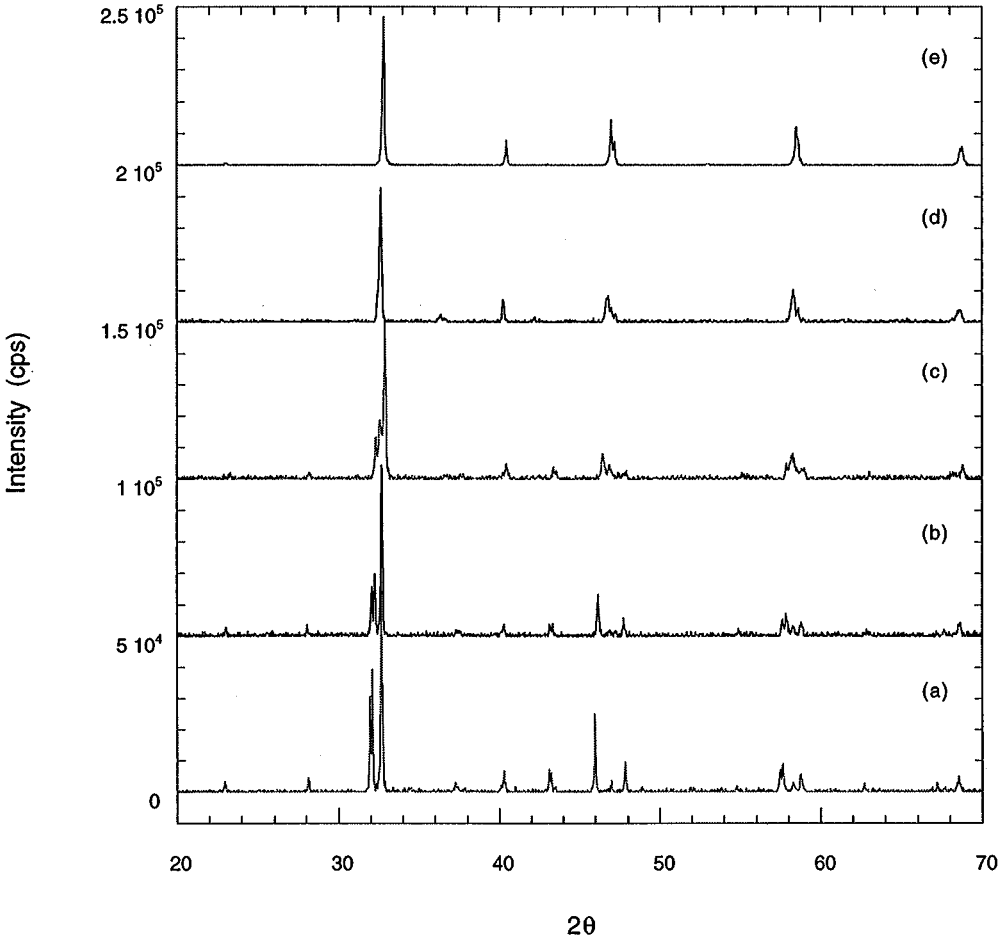

FIG. 2. Room-temperature X-ray diffraction profiles of the 1200°C air-sintered samples: (a) $Sr_4Fe_6O_{13\pm\delta}$, (b) $Sr_4Fe_{4.8}Co_{1.2}O_{13\pm\delta}$, (c) $Sr_4Fe_4Co_2O_{13\pm\delta}$, (d) $Sr_4Fe_{3.2}Co_{2.8}O_{13\pm\delta}$, and (e) $SrFe_{0.8}Co_{0.2}O_{13-\delta}$.

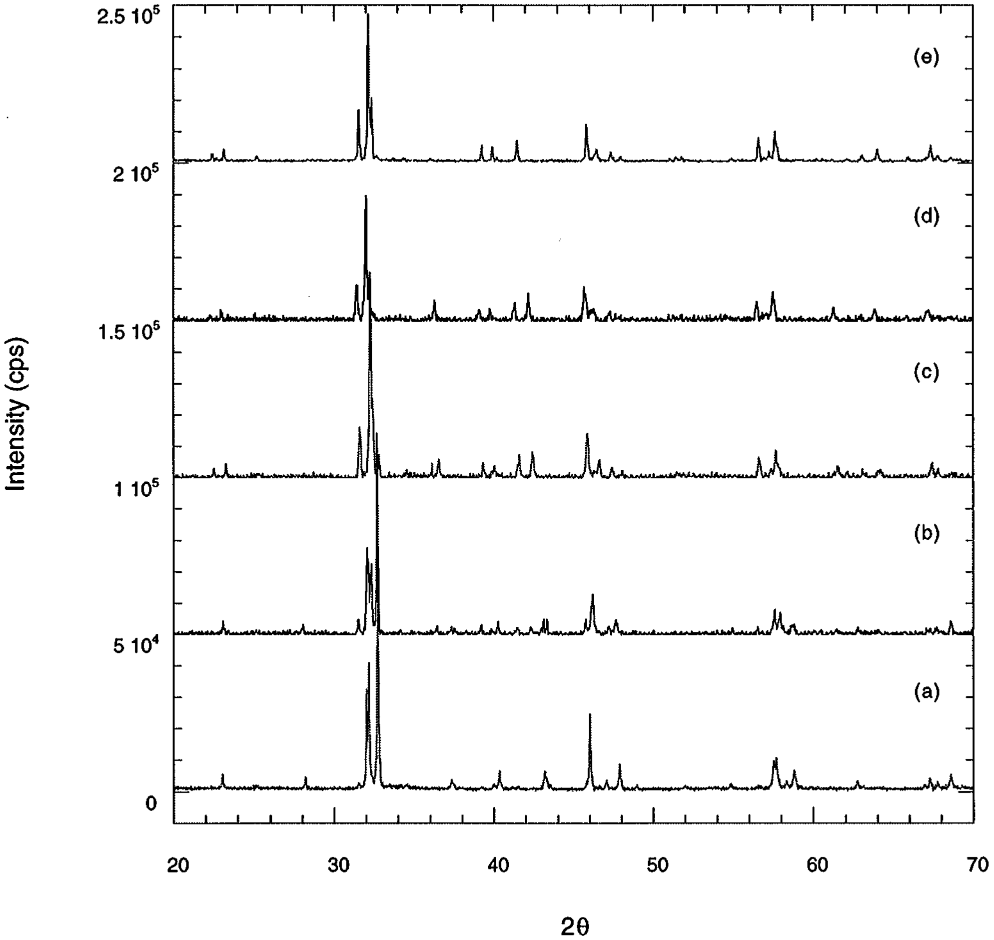

FIG. 3. Room-temperature X-ray diffraction profiles of the 1100°C argon-annealed samples: (a) $Sr_4Fe_6O_{13\pm\delta}$, (b) $Sr_4Fe_{4.8}Co_{1.2}O_{13\pm\delta}$, (c) $Sr_4Fe_4Co_2O_{13\pm\delta}$, (d) $Sr_4Fe_{3.2}Co_{2.8}O_{13\pm\delta}$, and (e) $Sr_2Fe_{1.6}Co_{0.4}O_5$.

amounts of perovskite $Sr(Fe_{1-u}Co_u)O_{3-\delta}$ and cobalt/iron oxides. The incorporation of cobalt into the structure of $Sr_4(Fe_{1-y}Co_y)_6O_{13\pm\delta}$ leads to a steady change in unit cell parameters with increasing cobalt doping (see Fig. 6). The $Sr_4(Fe_{1-y}Co_y)_6O_{13\pm\delta}$ unit cell volume gradually decreases with increasing cobalt substitution, as expected, since the ionic radius of the Co^{3+} cation, $r_i(VI) = 0.61$ Å, is less than $r_i(VI) = 0.645$ Å of the Fe^{3+} cation. The dependence of unit cell volume on x, the nominal cobalt content, determined here compares well with that determined by Guggilla and Manthiram (19) for $Sr_4(Fe_{1-y}Co_y)_6O_{13\pm\delta}$ ($y = 0, 0.1, 1.2$, and 0.25) (see Fig. 6). This agreement indicates that for the $Sr_4(Fe_{1-y}Co_y)_6O_{13\pm\delta}$ component in our samples the amount of cobalt substitution is equal to the nominal cobalt substitution attempted, i.e., $y = x$.

The sample of highest cobalt substitution attempted, with $x = 0.467$, was found to contain $Sr(Fe_{1-u}Co_u)O_{3-\delta}$ perovskite and cobalt/iron oxides but no amount of the layered $Sr_4(Fe_{1-y}Co_y)_6O_{13\pm\delta}$ phase of interest. The various phase compositions of the $Sr_4(Fe_{1-x}Co_x)_6O_{13\pm\delta}$ samples synthesized are summarized in Table 1.

Representative powder X-ray diffraction profiles of argon-annealed $Sr_4(Fe_{1-x}Co_x)_6O_{13\pm\delta}$ samples are shown in Fig. 3. The diffraction data show little difference between the air-sintered and argon-annealed samples of $Sr_4Fe_6O_{13\pm\delta}$, indicating that the crystal structure remains unchanged. For the cobalt-substituted samples $Sr_4(Fe_{1-x}Co_x)_6O_{13\pm\delta}$ ($x =$ 0.1, 0.2, 0.333, and 0.467), however, which contain varying amounts of perovskite, the perovskite $Sr(Fe_{1-u}Co_u)O_{3-\delta}$ phase converts to brownmillerite $Sr_2(Fe_{1-u}Co_u)_2O_5$ upon annealing in argon, $p_{O_2} \approx 10^{-6}$ atm. This phase conversion results from oxygen loss during annealing, which increases the amount of oxygen vacancies in $Sr(Fe_{1-u}Co_u)O_{3-\delta}$ to $\delta = 0.5$ and the ordering of these vacancies as the sample cools upon completion of the annealing stage. These oxygen vacancies become ordered into lines along the $[101]_p$ direction of the parent perovskite in every other $(0k0)_p$ plane, giving rise to alternate sheets of Fe/Co–oxygen tetrahedra

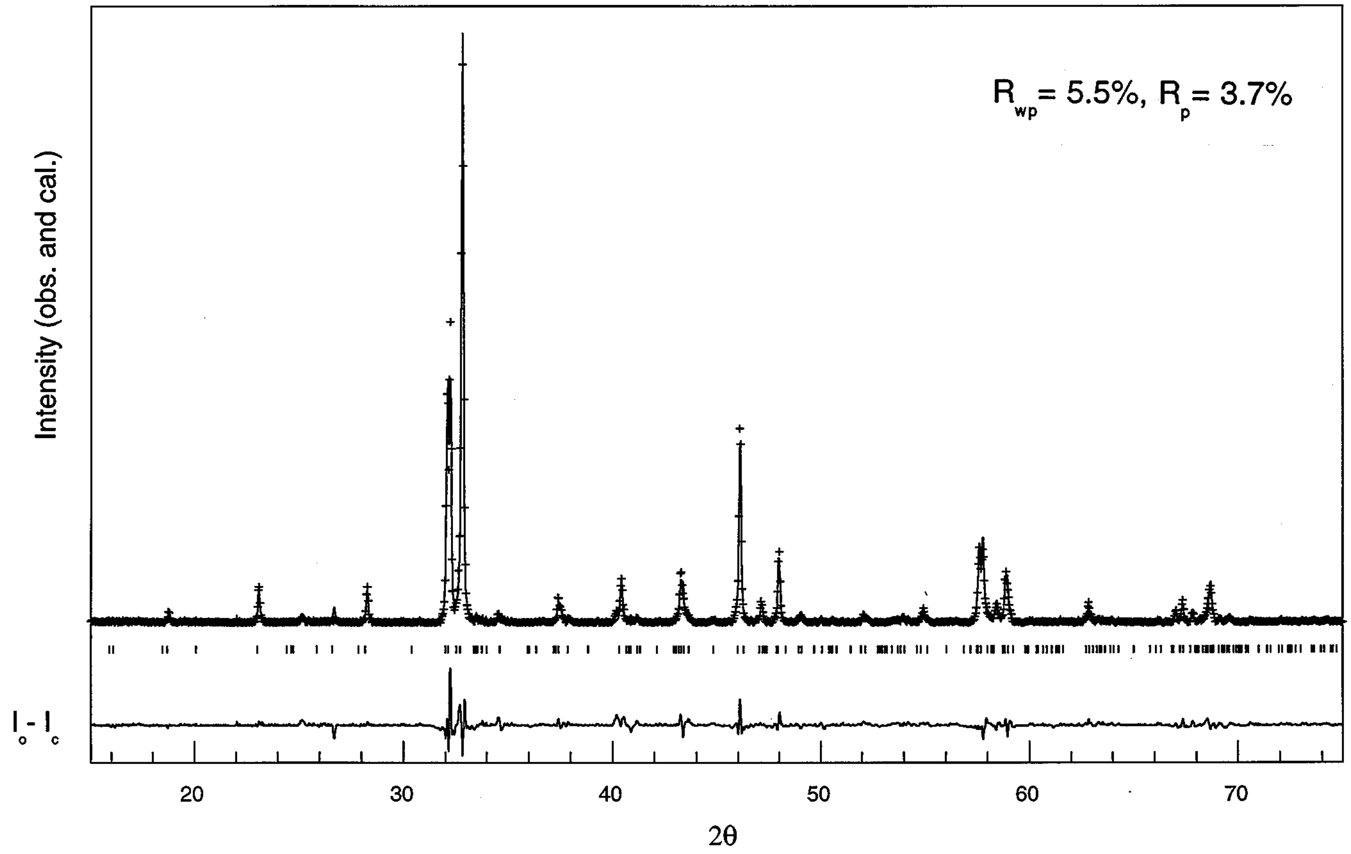

FIG. 4. Rietveld profile fit to powder X-ray diffraction data of $Sr_4Fe_6O_{13\pm\delta}$ sample. Observed, calculated, and difference profiles are shown along with reflection markers.

and octahedra (20). Schematic representations of the crystal structures of both perovskite and brownmillerite are shown in Fig. 7. The amount of brownmillerite phase present in the argon-annealed samples increases with x, the cobalt content, as shown in Figs. 3b, 3c, and 3d. The X-ray diffraction profile of $Sr_2Fe_{1.6}Co_{0.4}O_5$, a pure brownmillerite phase, is shown in Fig. 3e for comparison.

Scanning electron microscopy images of the air-sintered and argon-annealed $Sr_4Fe_4Co_2O_{13\pm\delta}$ sample are shown in Fig. 8; they reveal a dense structure for both samples. Energy-dispersive X-ray elemental analysis showed that the overall atomic ratio of the metal elements is consistent with that given in the nominal chemical formula, $Sr_4Fe_4Co_2O_{13\pm\delta}$. The polished-surface SEM images showed that the argon-annealed sample is denser and contains fewer pores than the air-sintered sample. A spherical cobalt-rich phase was observed in the argon-annealed sample. By correlating SEM observations with X-ray diffraction results, we identified the spherical phase as CoO.

The total conductivity of $Sr_4(Fe_{1-x}Co_x)_6O_{13\pm\delta}$ samples increases with both temperature and cobalt substitution, as shown in Fig. 9. At 900°C, conductivity of $Sr_4Fe_4Co_2O_{13\pm\delta}$ is ≈ 20 and $\approx 6\ S\cdot cm^{-1}$ in flowing air and argon environments, respectively. The total conductivities of $Sr_4Fe_{4.8}Co_{1.2}O_{13\pm\delta}$ ($x = 0.2$) and $Sr_4Fe_6O_{13\pm\delta}$ are ≈ 10 and $\approx 0.6\ S\cdot cm^{-1}$, respectively, at 900°C in air. Ionic transference numbers ($t_{ion} = \sigma_{ion}/\sigma_{total}$) of $Sr_4Fe_4Co_2O_{13\pm\delta}$ and $Sr_4Fe_{4.8}Co_{1.2}O_{13\pm\delta}$ are shown in Fig. 10 as a function of temperature in air. Ionic transference numbers for both samples were found to be largely temperature independent, with the higher ionic transference number being observed for the sample with lower cobalt content.

The measured EMFs on the sensor electrodes as a function of pumping current at various temperatures are plotted in Fig. 11. During all of our measurements, the gas-tight cell was surrounded with flowing dry air. To examine the contributions of bulk and interface effects to the oxygen permeation mechanism of the $Sr_4Fe_4Co_2O_{13\pm\delta}$ sample, we fitted the permeation data to the following equation (21):

$$j_{O_2} = \alpha[(p^{I}_{O_2})^r - (p^{II}_{O_2})^r], \qquad [3]$$

where r is the kinetic order in oxygen of the surface reaction and α is the exchange rate at $p_{O_2} = 1$ atm. For a permeation

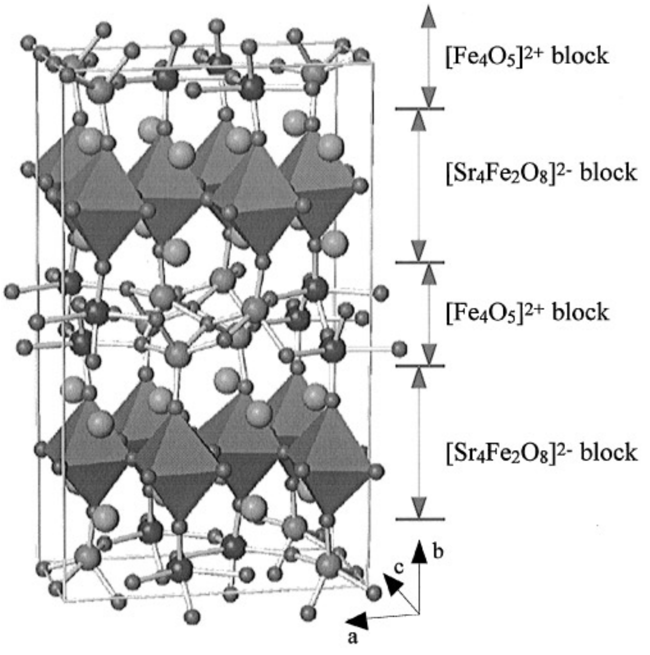

FIG. 5. Schematic representation of the $Sr_4Fe_6O_{13}$ crystal structure.

process where the surface reaction (exchange) effect is the controlling factor, we would have $r = 1/2$. The surface exchange constant α (in $cm \cdot min^{-1} \cdot atm^{-1/2}$) can be determined by a least-squares fitting of the experimental data. For the case where the bulk effect is the controlling factor, i.e., when the surface exchange rate is sufficiently large, oxygen permeation flux can be represented by (22)

$$j_{O2} = \frac{\beta}{L}[(p^{\mathrm{I}}_{O_2})^{1/4} - (p^{\mathrm{II}}_{O_2})^{1/4}], \qquad [4]$$

where L is the thickness of the membrane (in cm) and β is the bulk oxygen diffusion parameter (in $cm^2 \cdot min^{-1} \cdot atm^{-1/4}$). Figure 12 shows typical oxygen permeation data as a function of the p_{O_2} inside the cell, along with the least-squares fittings to Eq. [3] (with $r = 0.5$ and 0.25). The data fitting indicates that bulk diffusion plays the dominant role in the oxygen permeation process in the $Sr_4Fe_4Co_2O_{13\pm\delta}$ membrane of thickness ≈ 1 mm at high temperatures (> 650°C).

In Fig. 13, the steady-state oxygen permeation flux of a 2.9-mm-thick pellet specimen at 900°C (determined by solving Eq. [2]) is plotted as a function of the p_{O_2} inside the gas-tight cell. Figure 13 shows that the oxygen flux, j_{O_2}, increases dramatically in the range $p_{O_2} = 0.21$ to $\approx 10^{-3}$ atm, after which the oxygen flux only gradually increases when the p_{O_2} inside the cell is reduced further. These measurements of the oxygen permeability at various p_{O_2} gradients and temperatures show that, as expected, the oxygen permeability increases with temperature and p_{O_2} difference. At 900°C, the measured oxygen permeability

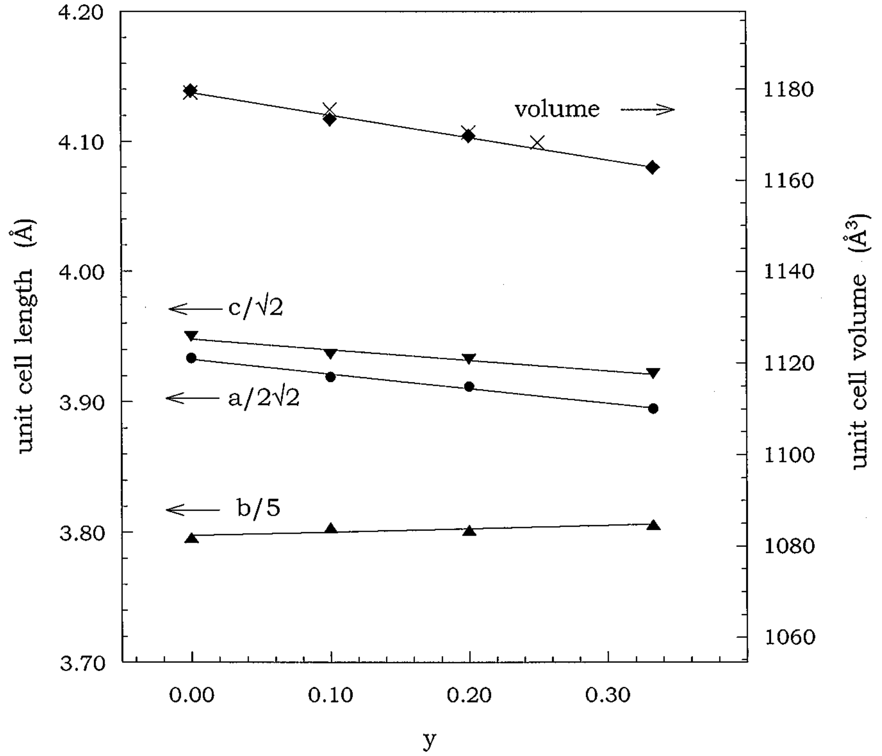

FIG. 6. Unit cell parameters of $Sr_4(Fe_{1-y}Co_y)_6O_{13\pm\delta}$ plotted as a function of cobalt substitution (solid symbols). Unit cell volumes determined by Guggilla and Manthiram (19) are also plotted (×).

TABLE 1
Phase Composition of Air-Sintered $Sr_4(Fe_{1-x}Co_x)_6O_{13\pm\delta}$ Samples and Unit Cell Parameters of the Component $Sr_4(Fe_{1-y}Co_y)_6O_{13\pm\delta}$ Phase

x	$Sr_4(Fe_{1-y}Co_y)_6O_{13\pm\delta}$	$Sr(Fe_{1-u}Co_u)O_{3-\delta}$	CoO[a]	a (Å)	b (Å)	c (Å)	V (Å^3)
0.0	> 98%			11.126	18.978	5.5864	1179.6
0.1	≈ 95%	≈ 4%		11.085	19.016	5.5670	1173.5
0.2	≈ 90%	≈ 8%		11.065	19.008	5.5618	1169.8
0.333	≈ 70%	≈ 25%	≈5%	11.017	19.030	5.5463	1162.8

[a] Deficiency in total wtf is attributed to remaining cobalt/iron oxides.

was $\approx 2.5\ \mathrm{scc \cdot cm^{-2} \cdot min^{-1}}$ for a 2.9-mm-thick membrane, and permeability increased as membrane thickness decreased.

Sintered thin-wall tubes of $Sr_4Fe_4Co_2O_{13\pm\delta}$ were tested in a methane conversion reactor for more than 1000 h (6, 7). An oxygen permeation flux of $\approx 10\ \mathrm{scc \cdot cm^{-2} \cdot min^{-1}}$ was observed for a 0.75-mm-thick tubular membrane (6). The oxygen permeation flux, determined from both reactor and gas-tight electrochemical cell experiments, is plotted in Fig. 14 as a function of reciprocal temperature. For comparison, the oxygen permeation flux of the disk membrane was normalized to that of a 0.75-mm-thick membrane. As can be seen, the oxygen permeation data obtained from these two independent experiments are in good agreement.

CONCLUSIONS

The phase composition of the $Sr_4(Fe_{1-x}Co_x)_6O_{13\pm\delta}$ samples was found to be strongly dependent on cobalt content. The $Sr_4Fe_6O_{13\pm\delta}$ sample is a single-phase material, whereas the cobalt-containing samples are multiphase. The amount of $Sr(Fe_{1-u}Co_u)O_{3-\delta}$ perovskite phase in the cobalt-containing samples increases disproportionately with x. In a reducing argon environment, the single-phase $Sr_4Fe_6O_{13\pm\delta}$ sample retained the same basic crystal structure as the air-sintered sample, whereas conversion of $Sr(Fe_{1-u}Co_u)O_{3-\delta}$ perovskite to brownmillerite $Sr_2(Fe_{1-u}Co_u)_2O_5$ phase was observed in the cobalt-containing samples.

The total conductivity of $Sr_4(Fe_{1-x}Co_x)_6O_{13\pm\delta}$ was found to increase with temperature and cobalt doping. At 900°C, the conductivity of $Sr_4Fe_4Co_2O_{13\pm\delta}$ is ≈ 20 and $\approx 6\ \mathrm{S \cdot cm^{-1}}$ in flowing air and argon environments, respectively, whereas the conductivities of $Sr_4Fe_{4.8}Co_{1.2}O_{13\pm\delta}$ and $Sr_4Fe_6O_{13\pm\delta}$ are ≈ 10 and $\approx 0.6\ \mathrm{S \cdot cm^{-1}}$, respectively, at 900°C in air. The ionic transference numbers of $Sr_4Fe_4Co_2O_{13\pm\delta}$ and $Sr_4Fe_{4.8}Co_{1.2}O_{13\pm\delta}$ were observed to be largely independent of temperature above 600°C in air. Higher total conductivity but lower ionic transference number was observed for the $Sr_4Fe_4Co_2O_{13\pm\delta}$ sample when compared with $Sr_4Fe_{4.8}Co_{1.2}O_{13\pm\delta}$. The oxygen permeation mechanism in the sintered $Sr_4Fe_4Co_2O_{13\pm\delta}$ material was found to be bulk controlled. At 900°C, an oxygen permeability of $\approx 2.5\ \mathrm{scc \cdot cm^{-2} \cdot min^{-1}}$ was observed in a 2.9-mm-thick membrane. This value agrees with values obtained in methane conversion reactor experiments (7).

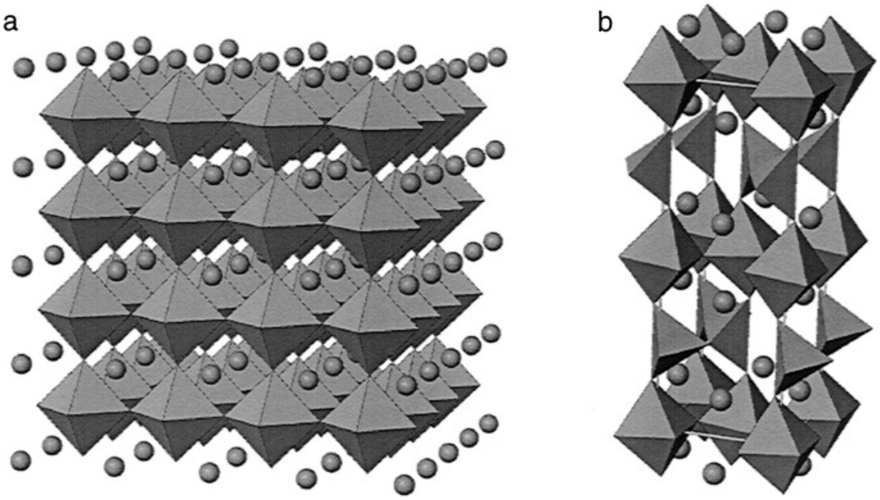

FIG. 7. Schematic representations of (a) perovskite and (b) brownmillerite crystal structures.

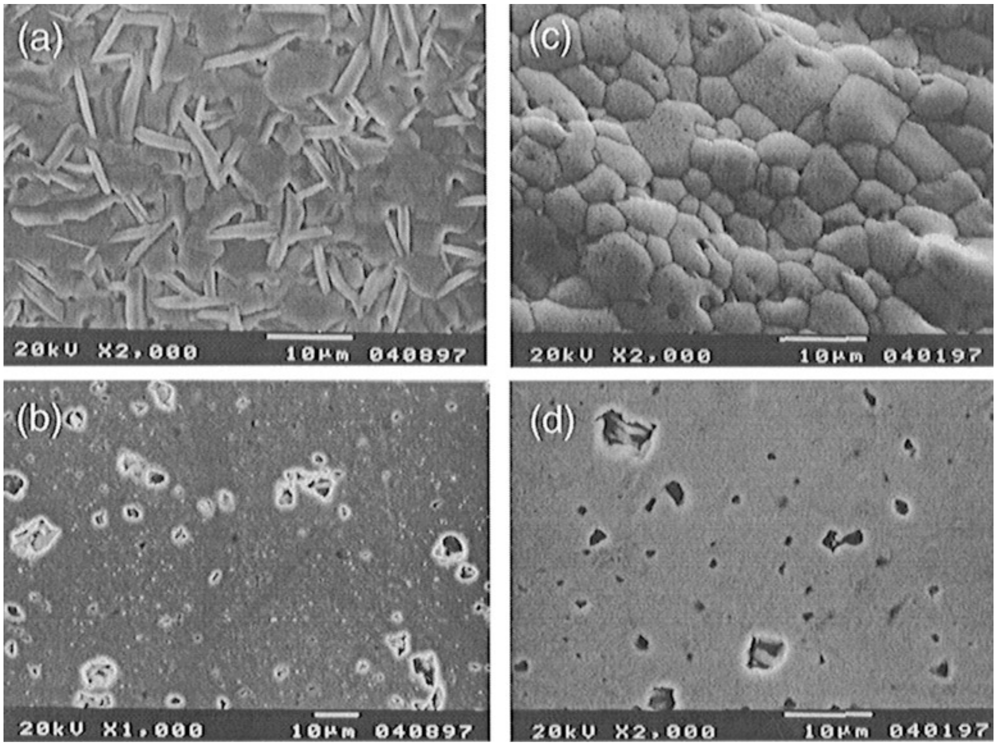

FIG. 8. SEM morphology of $Sr_4Fe_4Co_2O_{13\pm\delta}$ sample: (a) original surface of air-sintered sample; (b) polished surface of air-sintered sample; (c) original surface of argon-annealed sample; (d) polished surface of argon-annealed sample.

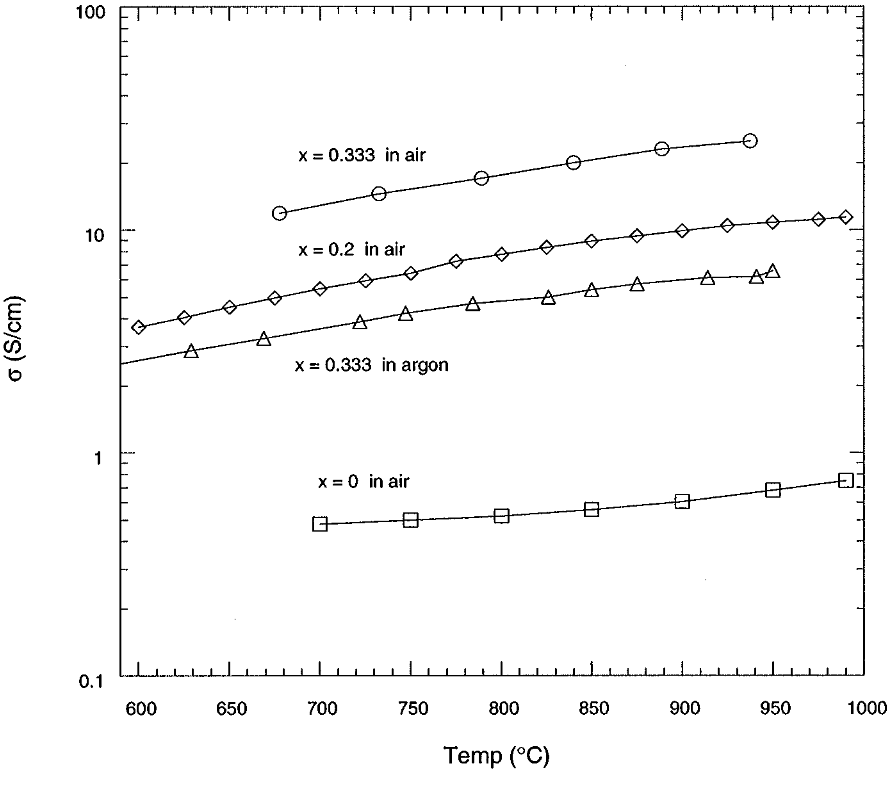

FIG. 9. Total conductivity of $Sr_4(Fe_{1-x}Co_x)_6O_{13\pm\delta}$ samples plotted as a function of temperature.

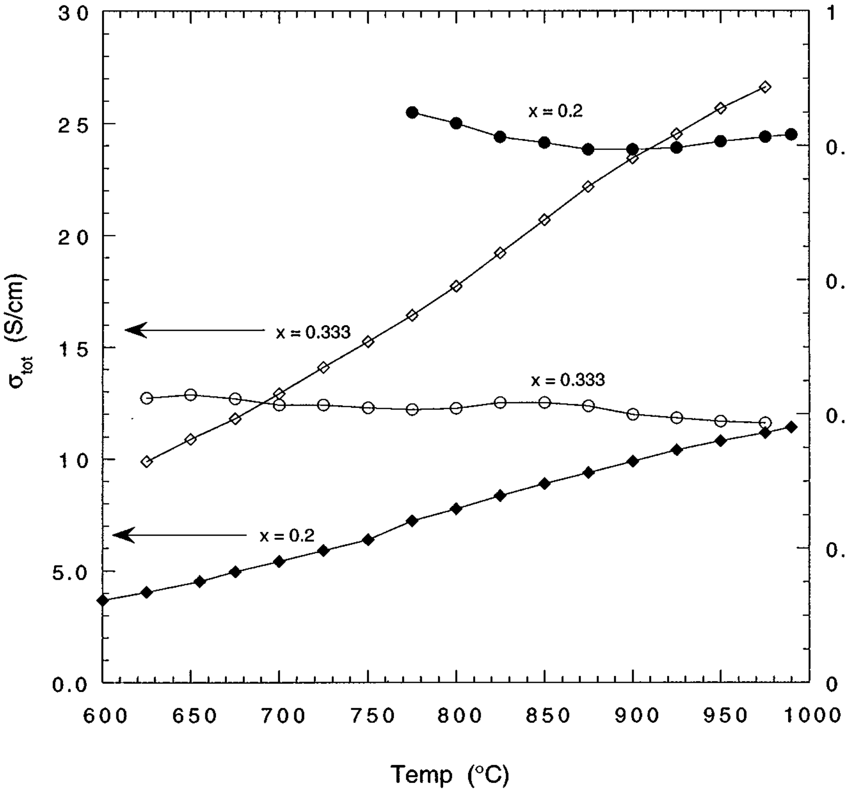

FIG. 10. Temperature dependence of ionic transference numbers of $Sr_4Fe_4Co_2O_{13\pm\delta}$ and $Sr_4Fe_{4.8}Co_{1.2}O_{13\pm\delta}$ samples.

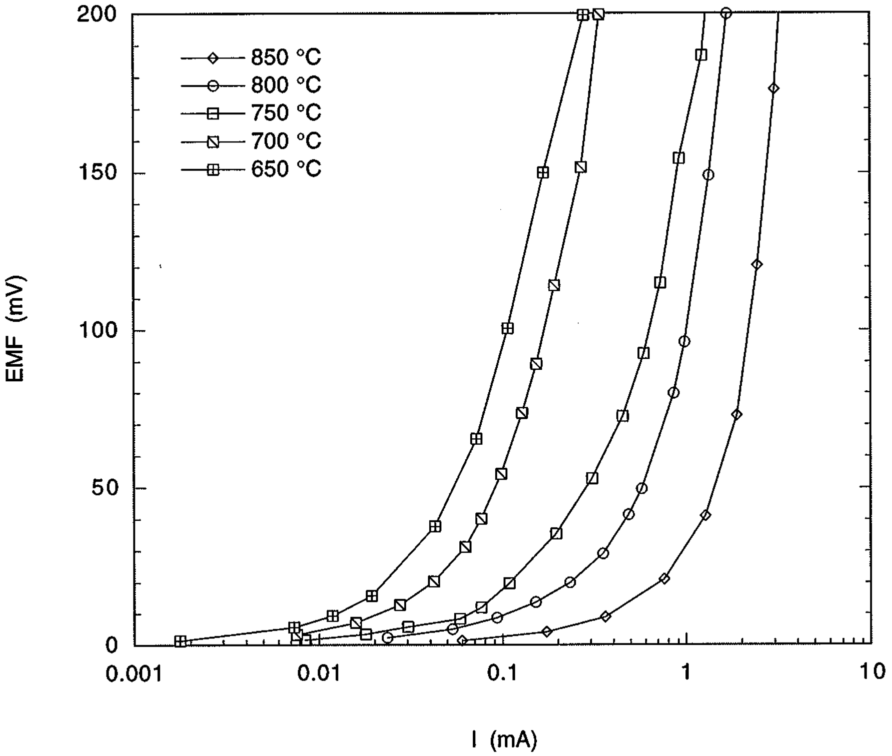

FIG. 11. Measured electromotive force as a function of pumping current at various temperatures.

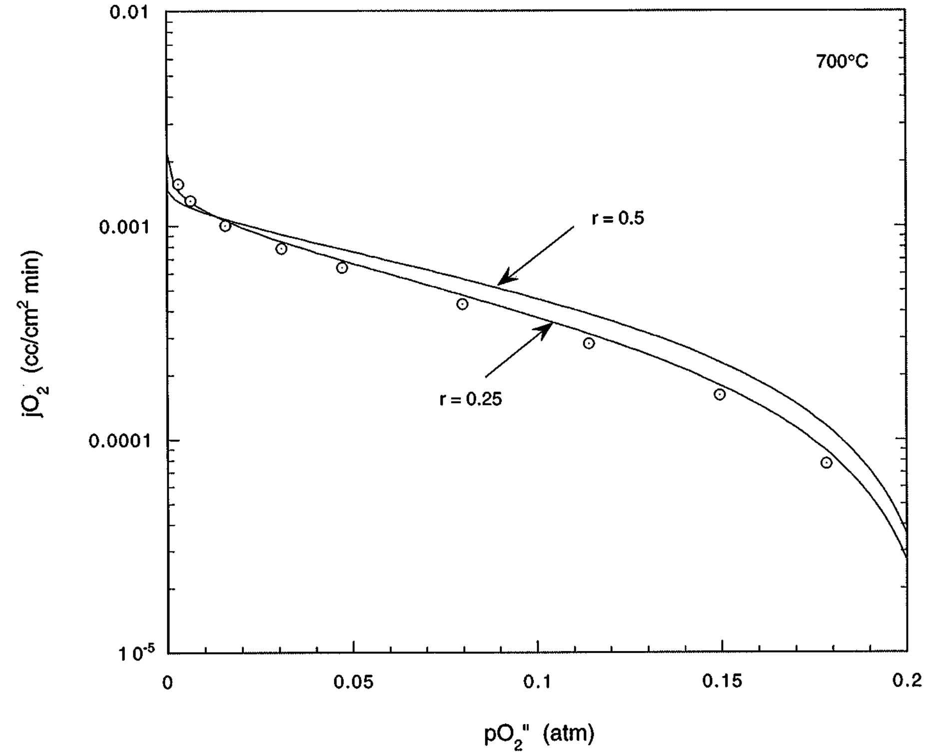

FIG. 12. Steady-state oxygen permeation flux as a function of p_{O_2} inside gas-tight cell and its fitting to Eq. [3] for $r = 0.5$ and 0.25.

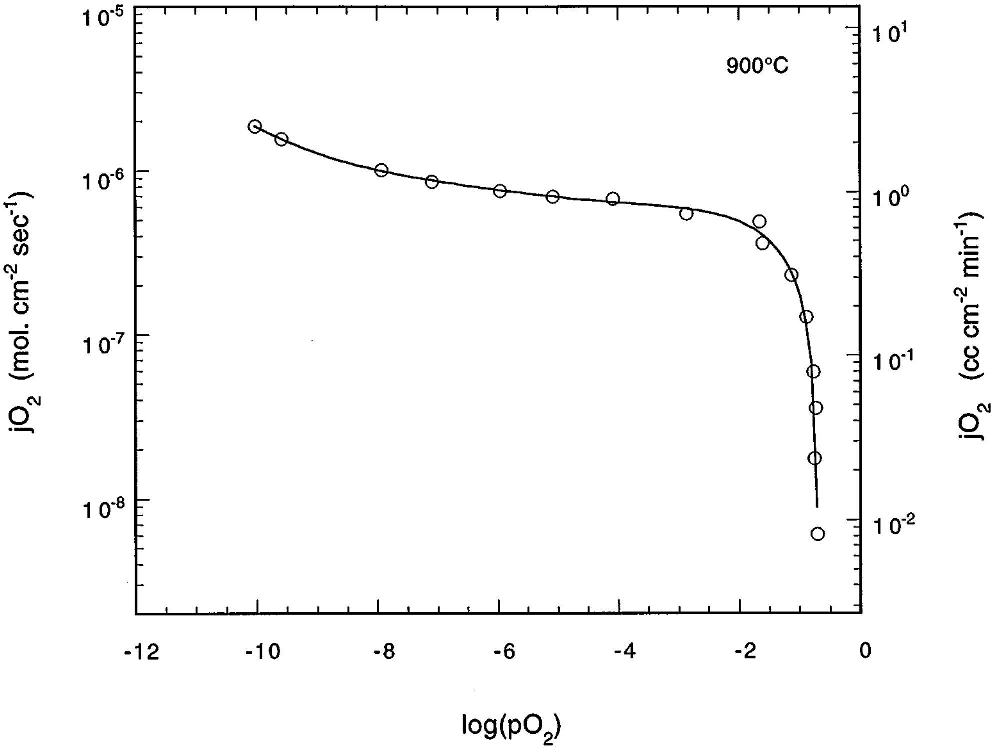

FIG. 13. Steady-state oxygen permeation flux for 2.9-mm-thick disk membrane plotted as a function of p_{O_2}.

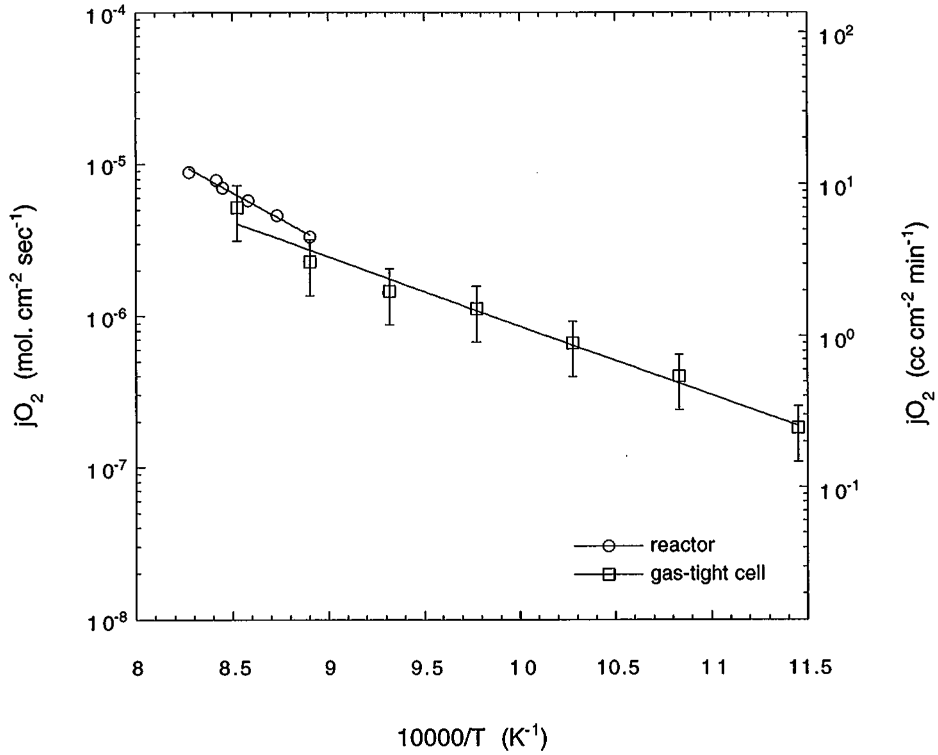

FIG. 14. Temperature dependence of oxygen permeation flux obtained from methane conversion reactor and gas-tight cell.

ACKNOWLEDGMENT

Work at Argonne National Laboratory is supported by the U.S. Department of Energy, Federal Energy Technology Center, under Contract W-31-109-Eng-38.

REFERENCES

1. T. Takahashi and H. Iwahara, *Energy Convers.* **11,** 105 (1971).
2. B. C. H. Steele, *Mater. Sci. Eng.* **13,** 79 (1992).
3. N. Q. Minh, *J. Am. Ceram. Soc.* **76,** 563 (1993).
4. R. DiCosimo, J. D. Burrington, and R. K. Grasselli, *J. Catal.* **102,** 377 (1992).
5. K. R. Kendall, C. Navas, J. K. Thomas, and H.-C. Loye, *Solid State Ionics* **82,** 215 (1995).
6. U. Balachandran, S. L. Morissette, J. T. Dusek, R. L. Mieville, R. B. Poeppel, M. S. Kleefisch, S. Pei, T. P. Kobylinski, and C. A. Udovich, "Proceedings of the Coal Liquefaction and Gas Conversion Contractor Review Conference" (S. Rogers *et al.*, Eds.), Vol. 1, pp. 138–160. U.S. Department of Energy, Pittsburgh Energy Technology Center, 1993.
7. U. Balachandran, T. J. Dusek, S. M. Sweeney, R. B. Poeppel, R. L. Mieville, P. S. Maiya, M. S. Kleefisch, S. Pei, T. P. Kobylinski, C. A. Udovich, and A. C. Bose, *Am. Ceram. Soc. Bull.* **74,** 71 (1995).
8. Y. Teraoka, H. M. Zhang, S. Furukawa, and N. Yamozoe, *Chem. Lett.* 1734 (1985).
9. Y. Teraoka, T. Nobunaga, and N. Yamazoe, *Chem. Lett.* 503 (1988).
10. B. Ma, J.-H. Park, C. U. Segre, and U. Balachandran, *Mater. Res. Soc. Symp. Proc.* **393,** 49 (1995).
11. B. Ma, U. Balachandran, C.-C. Chao, J.-H. Park, and C. U. Segre, *Ceram. Trans. Ser.* **73,** 169 (1997).
12. U. Balachandran, J. T. Dusek, P. S. Maiya, R. L. Mieville, B. Ma, M. S. Kleefisch, and C. A. Udovich, Presented at the 11th Intersociety Cryogenic Symposium, Energy Week Conference & Exhibition, Houston, Jan 28–30, 1997.
13. S. Pei, M. S. Kleefisch, T. P. Kobylinski, J. Faber, C. A. Udovich, V. Zhang-McCoy, B. Dabrowski, U. Balachandran, R. L. Mieville, and R. B. Poeppel, *Catal. Lett.* **30,** 201 (1995).
14. H. Iwahara, H. Uchida, K. Morimoto, and S. Hosgoi, *J Appl. Electrochem.* **19,** 448 (1989).
15. H. M. Rietveld, *J. Appl. Crystallogr.* **2,** 65 (1969).
16. A. C. Larson and R. B. Von Dreele, "General Structure Analysis Systems," Los Alamos Internal Report No. 86-748, 1986–1990.
17. A. Yoshiasa, K. Ueno, F. Kanamaru, and H. Horiuchi, *Mater. Res. Bull.* **21,** 175 (1986).
18. JCPDS—International Centre for Diffraction Data, No. 9-402 and 6-615.
19. S. Guggilla and A. Manthiram, *J. Electrochem. Soc.* **144,** L120 (1997).
20. C. Greaves, A. J. Jacobson, B. C. Tofield, and B. E. F. Fender, *Acta Crystallogr., Sect. B* **31,** 641 (1975).
21. H. J. M. Bouwmeester, H. Kruidhof, A. J. Burggraaf, and P. J. Gellings, *Solid State Ionics* **53–56,** 460 (1992).
22. S. Dou, C. R. Masson, and P. D. Pacey, *J. Electrochem. Soc.* **132,** 1843 (1985).